

Neural Network Attribution Methods for Problems in Geoscience: A Novel Synthetic Benchmark Dataset

Antonios Mamalakis, Imme Ebert-Uphoff, and Elizabeth A. Barnes

This work has been submitted to the *IEEE Transactions on Neural Networks and Learning Systems* for possible publication in the special issue entitled “Deep Learning for Earth and Planetary Geosciences.” Copyright may be transferred without notice, after which this version may no longer be accessible.

Abstract—Despite the increasingly successful application of neural networks to many problems in the geosciences, their complex and nonlinear structure makes the interpretation of their predictions difficult, which limits model trust and does not allow scientists to gain physical insights about the problem at hand. Many different methods have been introduced in the emerging field of eXplainable Artificial Intelligence (XAI), which aim at attributing the network’s prediction to specific features in the input domain. XAI methods are usually assessed by using benchmark datasets (like MNIST or ImageNet for image classification), or through deletion/insertion techniques. In either case, however, an objective, theoretically-derived ground truth for the attribution is lacking, making the assessment of XAI in many cases subjective. Also, benchmark datasets for problems in geosciences are rare. Here, we provide a framework, based on the use of additively separable functions, to generate attribution benchmark datasets for regression problems for which the ground truth of the attribution is known *a priori*. We generate a long benchmark dataset and train a fully-connected network to learn the underlying function that was used for simulation. We then compare estimated attribution heatmaps from different XAI methods to the ground truth in order to identify examples where specific XAI methods perform well or poorly. We believe that attribution benchmarks as the ones introduced herein are of great importance for further application of neural networks in the geosciences, and for accurate implementation of XAI methods, which will increase model trust and assist in discovering new science.

Index Terms— explainable artificial intelligence (XAI), neural networks (NNs), geosciences, regression problems, attribution benchmark, ground truth, additively separable functions.

I. INTRODUCTION

WITHIN the last decade, neural networks (NNs) [1] have seen tremendous application to the field of geosciences [2]-[10], owing in part to their impressive performance in capturing nonlinear system behavior [1], and the increasing

availability of observational and simulated data [11]-[14]. However, due to their complex structure, NNs are difficult to interpret (the so-called “black box” model). This limits their reliability and applicability since scientists cannot verify when a prediction is successful for the right reasons (i.e., they cannot test against “clever Hans” prediction models [15]) or better design a model that performs poorly (see for example [16]). Also, when applying NNs to new problems, the interpretability problem does not allow scientists to gain physical insights about the connections between the input variables and the prediction, and generally about the problem at hand. To address the interpretability problem, many different methods have been developed in recent years [17]-[26] in the emerging field of post hoc eXplainable Artificial Intelligence (XAI) [27]-[29]. These methods aim at a post hoc attribution of the prediction of a NN to specific features in the input domain (usually referred to as attribution/relevance heatmaps, saliency maps), thus highlighting relationships that may be interpreted physically, and making the “black box” more transparent [30]. Given that physical understanding is highly desirable to accompany any successful model in the geosciences, XAI methods are expected to be a real game-changer for further application of NNs in this field [31]-[32].

Despite their high potential, many XAI methods have been shown to not honor desirable properties (e.g., “completeness” or “implementation invariance”; see [23]), and in general, face nontrivial limitations for specific problem setups [33]-[36]. Thus, thorough investigation and assessment of XAI methods is of vital importance to be reliably applied in new scientific problems. So far, the assessment of the outputs of different XAI methods in geoscientific research (and in computer science) has been mainly based on applying these methods to benchmark problems, where the scientist is expected to know what the attribution heatmaps should look like, thus being able to judge the performance of the XAI method in question. Examples of benchmark problems for the geosciences include the classification of El Niño or La Niña years or seasonal prediction of regional hydroclimate [10],[31]. In computer science, commonly used benchmark datasets for image classification problems include MNIST or ImageNet among others [37]-[38]. A second way to assess the output of an XAI method is through deletion/insertion techniques [39]-[41], where highlighted

Submitted March 11, 2021. This work was supported in part by the National Science Foundation under Grant No. OAC-1934668 (all authors) and Grant No. ICER-2019758 (IE). (Corresponding Author: Antonios Mamalakis)

Antonios Mamalakis and Elizabeth A. Barnes are with the Department of Atmospheric Science, Colorado State University, Fort Collins, CO 80523 USA (e-mail: amamalak@rams.colostate.edu; ebarnes@rams.colostate.edu).

Imme Ebert-Uphoff is with the Department of Electrical and Computer Engineering, and the Cooperative Institute for Research in the Atmosphere, Colorado State University, Fort Collins, CO 80523 USA (e-mail: iebert@colostate.edu).

features are deleted from the full image (or added to a grey image). If the XAI method has highlighted the “correct” features, then the classification performance of the network is expected to decrease (improve) as important features are being deleted (added).

Although the above are good ways to gain insight about the performance of different XAI methods, there are some pitfalls in both cases. The deletion/insertion technique on its own does not give any insight into which features have been rightfully/falsefully highlighted or which features have been rightfully/falsefully ignored by the XAI method. Thus, the scientist can only assess the relative performance of different XAI methods, without understanding where the high/poor performance comes from; no ground truth is available. When using standard benchmark datasets (without exact attribution ground truth), the scientist is able to gain some general insight about what the XAI method is doing right/wrong. Yet, this is always based on the scientist’s subjective visual inspection of the result and their prior knowledge and understanding of the problem at hand, which involves high risks of cherry-picking specific samples/methods and reinforcing individual biases [42]. In other words, although it might make sense that an XAI method highlights the ears or the nose of a cat for an image successfully classified as “cat”, there is no objective truth about the relative importance of these two features to the prediction or the importance of other characteristics of the cat (e.g. its feet). The actual relative importance of different features is always case- or dataset-dependent, and the scientist can only get a general but not detailed view about the performance of the XAI method. Moreover, benchmark datasets that refer to regression problems are very rare, which is problematic, since many geoscientific applications can be approached as regression rather than classification problems.

Given the above and with the aim of a more falsifiable XAI research [42], in this paper we provide, for the first time, a framework to generate nonlinear benchmark datasets for geoscientific problems and beyond, where the importance of each input feature to the prediction is objectively derivable and known *a priori*. This *a priori* known attribution for each sample can be used as ground truth for evaluating different XAI methods and identifying examples where they perform well or poorly. We refer to such synthetic datasets as “attribution benchmark datasets”, to distinguish from benchmarks where no ground truth of the attribution is available. Our framework is outlined here for regression problems (but can be extended into classification problems too), where the input is a 2D field (i.e., a single-channel image); commonly found in geoscientific applications (e.g., [10],[31],[43],[44]).

We describe our synthetic framework and generate an attribution benchmark in Section II. Next we train a fully-connected NN on the synthetic dataset and apply different XAI methods to estimate the model attributions (Section III). We

compare the estimated attributions with the ground truth in order to thoroughly and objectively assess the performance of the XAI methods considered here (Section IV). In Section V, we state our conclusions.

II. A NONLINEAR ATTRIBUTION BENCHMARK DATASET

Let us consider the illustrative problem of predicting regional climate from global 2D fields of sea surface temperature (SST; see e.g., [43]-[44]). The general idea of this paper is summarized in Fig. 1. We start by generating N realizations of an input random vector $\mathbf{X} \in \mathbb{R}^d$ (e.g., N synthetic samples of a vectorized 2D SST field). We use a nonlinear function $F: \mathbb{R}^d \rightarrow \mathbb{R}$, which represents the physical system of our problem setting (e.g., the climate system), to map each realization \mathbf{x}_n into a scalar y_n , and generate the output random variable Y (e.g., regional climatic variable). We then train a fully-connected NN to approximate the underlying function F and compare the model attributions estimated by different XAI methods with the ground truth in order to thoroughly and objectively assess their performance.

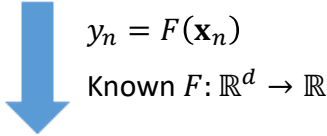
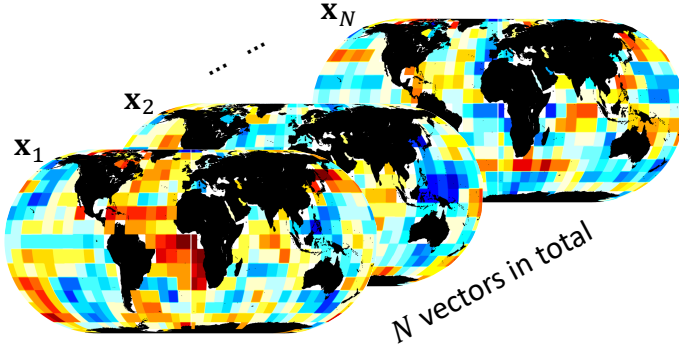
In this section, we describe how to generate synthetic datasets of the input \mathbf{X} and the output Y . Although here we present results for a climate prediction setting for illustration, our framework is generic and applicable to a large number of problem settings in the geosciences and beyond.

A. Input Variables

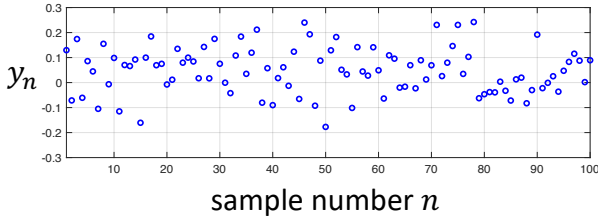
We start by randomly generating $N = 10^6$ independent realizations of an input vector $\mathbf{X} \in \mathbb{R}^d$. Although arbitrary, the distributional choice of the input is decided with the aim of being a reasonable proxy of the independent variable of the physical problem of interest. Here, the input series represent monthly global fields of SST anomalies (deviations from the seasonal cycle) at a $10^\circ \times 10^\circ$ resolution (fields of $d = 458$ variables; see step 1 in Fig. 1). We generate the SST anomaly fields from a multivariate Normal Distribution $\text{MVN}(\mathbf{0}, \mathbf{\Sigma})$, where $\mathbf{\Sigma}$ is the covariance matrix and represents the dependence between SST anomalies in different grid points (or pixels in image classification settings) around the globe (spatial dependence). The matrix $\mathbf{\Sigma}$ is set equal to the sample correlation matrix that is estimated from monthly SST observations². If a user wants to eliminate spatial dependence, then a good choice might be $\mathbf{\Sigma} = \sigma^2 I_d$, where σ^2 is the variance and I_d is the identity matrix. We note that we decided to generate a large amount of data $N = 10^6$ (much larger than what is usually available in reality), so that we can achieve a near perfect NN prediction accuracy, and make sure that any discrepancy between the estimated attributions and the ground truth comes from limitations of the corresponding XAI method and not from poor training.

²SST monthly fields are freely available online at: <https://psl.noaa.gov/data/gridded/data.cobe2.html>

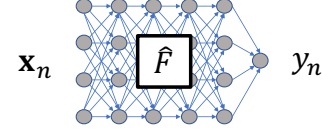
Step 1: Generate N samples of $\mathbf{X} \in \mathbb{R}^d$ from a MVN



Step 2: Use a known function F that maps each vector \mathbf{x}_n into a scalar y_n



Step 3: Pretend function F is not known and train a NN using inputs \mathbf{x}_n and outputs y_n



Step 4: Use XAI methods to look into the NN and compare with the ground truth

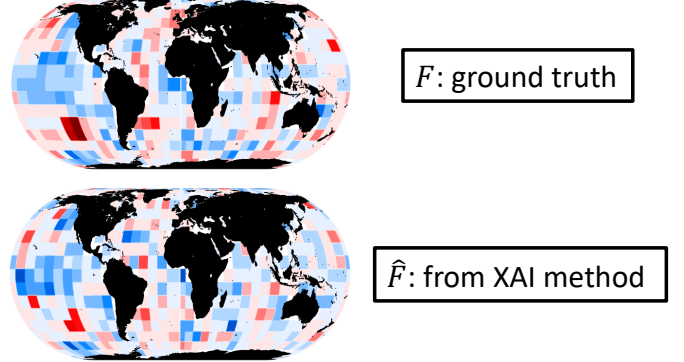


Fig. 1. Schematic overview of the general idea of the paper for a climate prediction setting. In step 1 (Section II), we generate N independent realizations of a random vector $\mathbf{X} \in \mathbb{R}^d$ from a multivariate Normal Distribution. In step 2 (also Section II), we generate a response $Y \in \mathbb{R}$ to the synthetic input \mathbf{X} , using a known nonlinear function F . In step 3 (Section III), we train a fully-connected NN using the synthetic data \mathbf{X} and Y to approximate the function F . The NN learns a function \hat{F} . Lastly, in step 4 (Section IV), we compare the attribution heatmaps estimated from different XAI methods to the ground truth (that represents the function F), which has been objectively derived for any sample $n = 1, 2, \dots, N$.

B. Synthetic Response based on Additively Separable Functions

We next create a nonlinear response $Y \in \mathbb{R}$ to the synthetic input $\mathbf{X} \in \mathbb{R}^d$ (see step 2 in Fig. 2), using a real function $F: \mathbb{R}^d \rightarrow \mathbb{R}$. For any sample $n = 1, 2, \dots, N$, the response of our system y_n to the input \mathbf{x}_n is given as $y_n = F(\mathbf{x}_n)$ or after dropping the index n for simplicity and relating the random variables instead of the samples, $Y = F(\mathbf{X})$.

Theoretically, the function F can be any function the user is interested to benchmark an NN against. However, in order for the final synthetic dataset to be useful as an attribution benchmark for XAI methods, function F needs to: i) have such a form so that the importance/contribution of each of the input variables to the response Y is objectively derivable, and ii) be nonlinear, as is the case in the majority of applications in geoscience.

The simplest form for F so that the above two conditions are honored is when F is an *additively separable function*, i.e. there exist local functions C_i , with $i = 1, 2, \dots, d$, so that:

$$F(\mathbf{X}) = F(X_1, X_2, \dots, X_d) = C_1(X_1) + C_2(X_2) + \dots + C_d(X_d) \quad (1)$$

where, X_i is the random variable at grid point i . Under this

setting, the response Y is the sum of local responses at grid points i , and although the local functions C_i may be independent from each other, one can also apply functional dependence by enforcing neighboring C_i to behave similarly, when the physical problem of interest requires it (see next subsection). Moreover, as long as the local functions C_i are nonlinear, so is the response Y , which satisfies our aim. Most importantly, with F being an additively separable function, the importance/contribution of each of the variables X_i to the response y_n for any sample n , is by definition equal to the value of the corresponding local function, i.e., $R_{i,n}^{true} = C_i(x_{i,n})$. This satisfies the basic desirable property that any response can be objectively attributed to the input.

Of course, this simple form of F comes with the pitfall that it may not be exactly representative of some complex physical problems. However, for this study we are not trying to capture all possible functional forms of F , but rather, provide a sample form of F that honors the two desirable properties for benchmarking XAI methods. We also note that by changing the form of local functions C_i (and the dimension d), one can create theoretically infinite different forms of F and of attribution benchmarks to test XAI methods against. Next, we define the local functions C_i that we use in this study.

C. Local Functions

The simplest form of the local functions is linear, i.e., $C_i(X_i) = \beta_i X_i$. In this case, the response Y falls back to a traditional linear regression response, which is not necessarily very interesting (there is no need to train a NN to describe a linear system), and it is certainly not representative of the majority of geoscience applications. More interesting responses to benchmark a NN or XAI methods against are responses where the local functions have a nonlinear form, e.g., $C_i(X_i) = \sin(\beta_i X_i + \beta_i^0)$, or $C_i(X_i) = \beta_i X_i^2$, etc.

In this study, to avoid prescribing the form of nonlinearity, we defined the local functions to be piece-wise linear (PWL) functions, with number of break points K , and with the condition $C_i(0) = 0$, for any grid point $i = 1, 2, \dots, d$. The latter leads to a reasonable condition for climate applications, that $y|_{x=0} = F(\mathbf{0}) = 0$, i.e., if the SST is equal to the climatological average, then the response Y is also equal to the climatological average. Our inspiration for using PWL functions is the use of ReLU (a piece-wise linear function with $K = 1$) as the activation function in NN architectures. Indeed, a piece-wise linear response can describe highly nonlinear behavior of any form as the value of K increases, frequently met in climate prediction settings. For example, it is well established in the climate literature that the response of the extratropical hydroclimate to the El Niño-Southern Oscillation is not linear, and the effect of El Niño and La Niña events on the extratropics is not symmetric [45]-[46]. Thus, in this study, we will generate the Y series using PWL local functions, but we note that benchmarking of XAI methods can also be performed using other types of additively separable responses.

A schematic example of a local piece-wise linear function C_i , for $K = 5$ that is used herein, is presented in Fig. 2. For each grid point i , the break points l_k , $k = 1, 2, \dots, K$ are obtained as the empirical quantiles of the synthetic series of X_i that correspond to probability levels chosen randomly from a uniform distribution (also, note that we enforce that the point $x = 0$ is always a break point). The corresponding slopes $\beta_i^1, \beta_i^2, \dots, \beta_i^{K+1}$ are chosen randomly by generating $K + 1$ realizations from a MVN($\mathbf{0}, \Sigma$), where Σ is again estimated from SST observations and is used to enforce spatial dependence in the local functions. In Fig. 2, the map of β_i^6 (the slope for $X_i \in (l_5, \infty)$) is shown for all grid points in the globe, and the local functions C_i for three points A, B, and C are also presented. First, the spatial coherence of the slopes β_i^6 is evident, with positive slopes over e.g., most of the northern Pacific and Indian Ocean and negative slopes over e.g., the eastern tropical Pacific. Second, the local functions at the neighboring points A and B are very similar to each other, consistent with the functional spatial dependence that we have specified. Lastly, the local function at point C very closely approximates a linear function. Indeed, in the way that the slopes $\beta_i^1, \beta_i^2, \dots, \beta_i^{K+1}$ are randomly chosen, it is possible that the local functions at some grid points end up being approximately linear. However, based on Monte Carlo simulations, we have established that the higher the value of K , the more unlikely it is to obtain approximately linear local functions (not shown).

Before moving forward, we wish to again highlight that although the total response Y is nonlinear and potentially very complex, the contributions of the input variables to the response are always known and equal to the corresponding local functions, simply because the function F is an additively separable function.

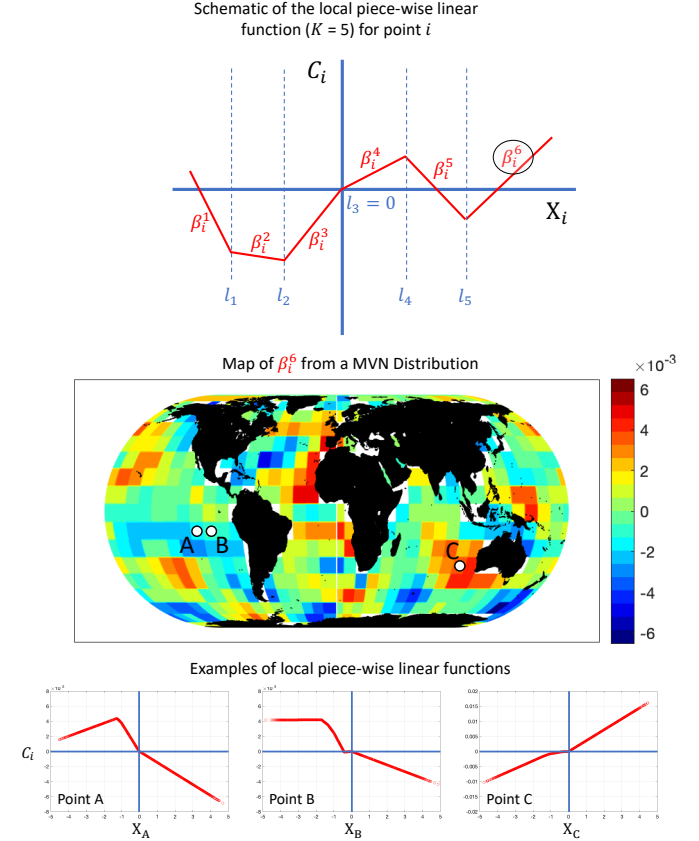


Fig. 2. Schematic representation and actual examples of local piece-wise linear functions C_i , for $K = 5$.

III. NEURAL NETWORK ARCHITECTURE AND XAI METHODS

So far, we generated $N = 10^6$ independent realizations of an input vector $\mathbf{X} \in \mathbb{R}^d$ (with $d = 458$) and of an output scalar response $Y \in \mathbb{R}$, using an additively separable function F , with PWL local functions and $K = 5$. Next, we train a fully connected NN to learn the function F (see step 3 in Fig. 1), using the first 900,000 samples for training and the last 100,000 samples for validation. Apart from assessing the prediction performance, the validation samples will also be used to assess the performance of different post hoc, local XAI methods that have been commonly used in the literature and that are defined below.

A. Neural Network

To approximate the function F , we used a fully connected NN (with ReLU activation functions), with six hidden layers, each one containing 512, 256, 128, 64, 32, and 16 neurons, respectively. We do not argue that this is the optimum architecture to approach the problem since this is not the focus of our study. Instead, what is important is to achieve high enough performance, so that any significant discrepancy between the attribution ground truth and the estimated

attributions does not come from a poor training, but rather from possible pitfalls of the XAI methods. The coefficient of determination of the NN prediction in the validation sample was slightly higher than $R^2 = 99\%$, which suggests that the NN can explain 99% of the variance in Y .

As a benchmark to the NN, we also trained a linear regression model. The performance of the linear model was much poorer, with $R^2 = 65\%$ for the validation data.

B. XAI Methods

We consider two different categories of local, post hoc XAI methods. The first category includes gradient-based methods.

1) Gradient: This method is among the simplest but very commonly used methods to explain an NN prediction. In this method, one simply calculates the partial derivative of the network's output with respect to each of the input variables X_i , at the specific sample in question. So, the relevance of the variable at grid point i to the network's prediction for the sample n , is:

$$R_{i,n} = \left. \frac{\partial \hat{F}}{\partial X_i} \right|_{x_i=x_{i,n}} \quad (2)$$

where \hat{F} is the function learned by the NN, as an approximation to the function F . This method estimates the sensitivity of the network's output to the input variable X_i . The motivation for using the Gradient method is that if changing the value, $x_{i,n}$, of a grid point in a given input sample is shown to cause a large difference in the NN output value, then that grid point might be important for the prediction. Furthermore, calculation of the Gradient is very convenient, as it is readily available in any neural network training environment, contributing to the method's popularity. However, as we will see in the next Section IV, the sensitivity is often *not* a good estimator of the contribution (saliency) of a variable to the prediction of the network.

2) Smooth Gradient: This method was introduced in [19] and is very similar to the method Gradient, except that it aims to obtain a more robust estimation of the local derivative by averaging the gradients over a perturbed number of inputs with added noise:

$$R_{i,n} = \frac{1}{m} \sum_{j=1}^m \left. \frac{\partial \hat{F}}{\partial X_i} \right|_{x_i=x_{i,n}+e_j} \quad (3)$$

where m is the number of perturbations, and e_j comes from a standard Normal Distribution.

3) Input*Gradient: As is evident from its name, in this method [17] one multiplies the local gradient with the input itself, to get the relevance:

$$R_{i,n} = x_{i,n} * \left. \frac{\partial \hat{F}}{\partial X_i} \right|_{x_i=x_{i,n}} \quad (4)$$

This method works perfectly for a linear \hat{F} , since for a linear model, the derivative is a constant, and the product of the slope

of the line with the input always gives the value of the true contribution to the total response. The Input*Gradient method is used in the majority of XAI studies due to its simplicity.

4) Integrated Gradients: This method [23] is similar to the Input*Gradient method, but aims to account for the fact that in nonlinear problems the derivative is not constant, and thus, the product of the local derivative with the input might not be a good approximation of the contribution. This method considers a reference (baseline) vector $\hat{\mathbf{x}} \in \mathbb{R}^d$, for which the network's output is zero, i.e., $\hat{F}(\hat{\mathbf{x}}) = 0$. Then the relevance is equal to the product of the distance of the input from the reference point with the average of the gradients at points along the straightline path from the reference point to the input:

$$R_{i,n} = (x_{i,n} - \hat{x}_i) * \frac{1}{m} \sum_{j=1}^m \left. \frac{\partial \hat{F}}{\partial X_i} \right|_{x_i=\hat{x}_i+\frac{j}{m}(x_{i,n}-\hat{x}_i)} \quad (5)$$

where m is the number of steps in the Riemann approximation.

The second category of methods that we consider includes different implementation rules of the Layer-wise Relevance Propagation (LRP) method [24],[47]. In the LRP method, one sequentially propagates the prediction $\hat{F}(\mathbf{x}_n)$ back to neurons of lower layers, obtaining intermediate relevances for all neurons until the input layer is reached and the relevances of the input $R_{i,n}$ are calculated.

5) LRP_z: In the first LRP rule we consider, the back propagation is performed as follows:

$$R_i^{(l)} = \sum_j \frac{z_{ij}}{z_j} R_j^{(l+1)} \quad (6)$$

where $R_j^{(l+1)}$ is the relevance of the neuron j at the upper layer $(l+1)$, and $R_i^{(l)}$ is the relevance of the neuron i at the lower layer (l) . The propagation is based on the ratio of the localized preactivations z_{ij} during prediction time and their respective aggregation $z_j = \sum_i z_{ij}$. Because this rule might lead to unbounded relevances as z_j approaches zero [24], additional advancements have been proposed.

6) LRP_{αβ}: In this rule [24], positive and negative preactivations z_{ij} are considered separately, so that the denominators are always nonzero:

$$R_i^{(l)} = \sum_j \left(\alpha \frac{z_{ij}^+}{z_j^+} + \beta \frac{z_{ij}^-}{z_j^-} \right) R_j^{(l+1)} \quad (7)$$

where

$$z_{ij}^+ = \begin{cases} z_{ij}^+ = z_{ij}; & z_{ij} > 0 \\ 0 & \end{cases} \quad z_{ij}^- = \begin{cases} 0 & \\ z_{ij}^- = z_{ij}; & z_{ij} < 0 \end{cases}$$

In our study, we use the commonly used rule with $\alpha = 1$ and $\beta = 0$, which considers only positive preactivations [24].

7) Deep Taylor Decomposition: For each neuron j at an upper layer $(l+1)$, this method [25] computes a rootpoint \hat{x}_i^j close to the input x_i , for which the neuron's output is zero, and uses the difference $(x_i - \hat{x}_i^j)$ to estimate the relevance of the

lower-layer neurons recursively. The relevance re-distribution is performed as follows:

$$R_i^{(l)} = \sum_j \frac{\partial R_j^{(l+1)}}{\partial x_i} \Big|_{x_i = \hat{x}_i^j} * (x_i - \hat{x}_i^j) \quad (8)$$

where $R_j^{(l+1)}$ is the relevance of the neuron j at the upper layer ($l + 1$), and $R_i^{(l)}$ is the relevance of the neuron i at the lower layer (l). It has been shown in [25],[47] that for NNs with ReLU activations, Deep Taylor leads to similar results to the $\text{LRP}_{\alpha=1, \beta=0}$ rule.

IV. RESULTS

In this section, we compare the attribution/relevance heatmaps estimated by the considered XAI methods to the ground truth (see step 4 in Fig. 1). Note that for a perfect NN and a perfect XAI method, the estimated heatmap should look exactly like the ground truth. Thus, the correlation coefficient (see also [34],[48]) of the estimated heatmap and the ground truth will serve as our metric to assess the performance of the

explanation. We first present results for specific samples in the validation, to get a qualitative insight on the XAI performance, and then we present more quantitative summary statistics of the performance across all samples from the validation set.

A. Illustrative Comparisons

In Fig. 3, we present the ground truth and the estimated relevance heatmaps from the considered XAI methods (each heatmap is standardized by the corresponding maximum absolute relevance within the map). This sample corresponds to a response $y_n = 0.0660$, while the NN predicts 0.0802. Based on the ground truth, features that contributed positively to the response y_n occur mainly over the eastern tropical and southern Pacific Ocean, and the southeastern Indian Ocean. Features with negative contribution occur over the Atlantic Ocean and mainly in the tropics.

Based on the method Gradient, the attribution of the NN prediction is not consistent at all with the ground truth. In the eastern tropical and southern Pacific Ocean, the method returns negative relevances instead of positive, and over the tropical Atlantic, positive relevances (instead of negative) are highlighted. The pattern correlation is very small on the

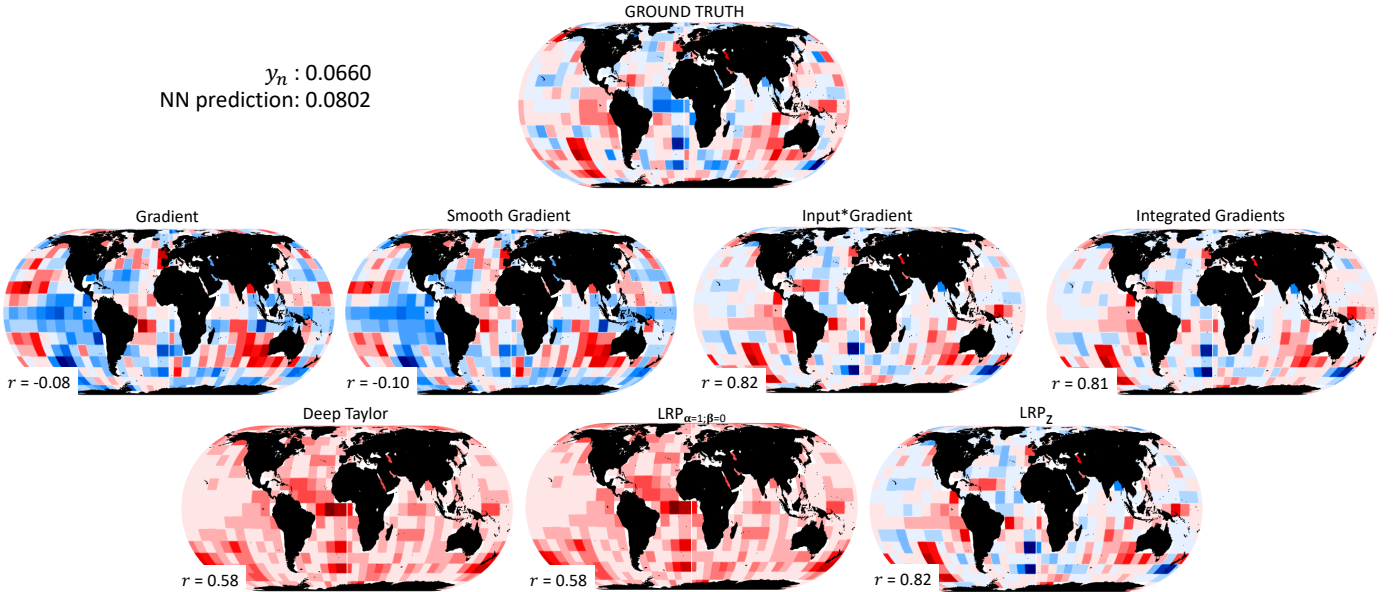


Fig. 3. Performance of different XAI methods for the sample $n = 979,476$ in the validation. The XAI performance is assessed by comparing the estimated heatmaps to the ground truth. All heatmaps are standardized with the corresponding maximum (in terms of absolute value) relevance. Red (blue) color corresponds to positive (negative) contribution to the response/prediction, with darker shading representing higher (in terms of absolute value) relevance. The correlation coefficient between each heatmap and the ground truth is also provided. Only for the methods Deep Taylor and $\text{LRP}_{\alpha=1, \beta=0}$ the correlation with the absolute ground truth is given.

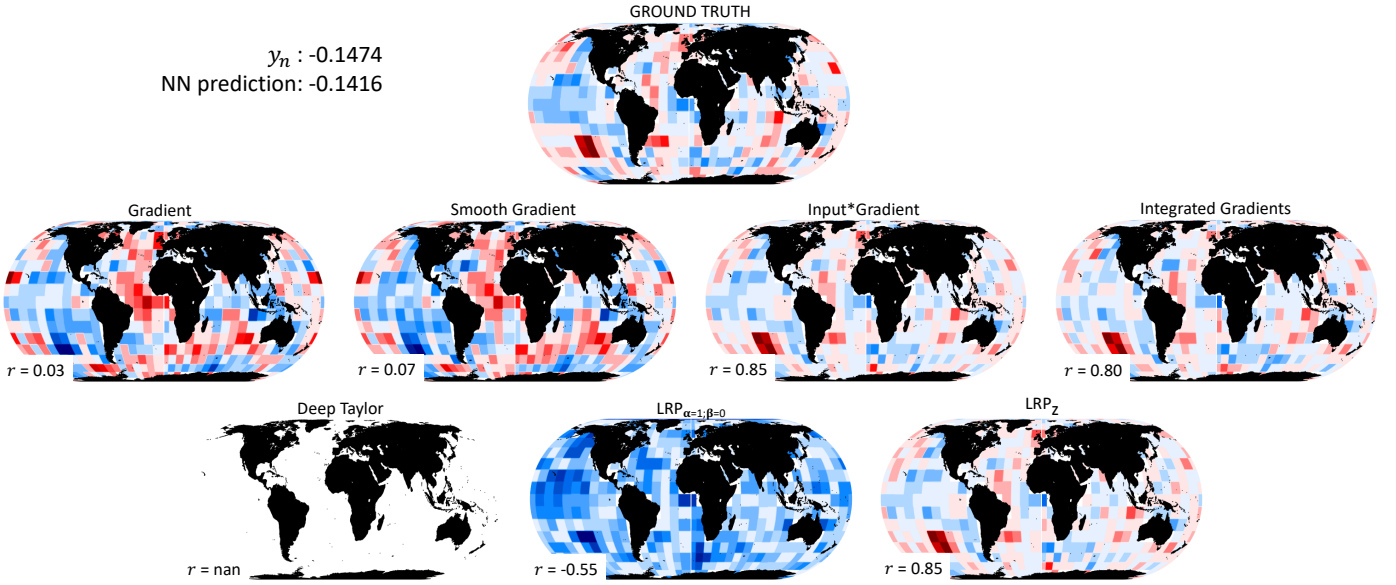


Fig. 4. Same as Fig. 3, but for the sample $n = 995,903$ in the validation.

order of -0.08 , consistent with the above observations. As theoretically expected, this result indicates that the *sensitivity* of the output to the input is not the same as the *contribution* of the output to the input [26]. The method Smooth Gradient performs poorly and similarly to the method Gradient, with a correlation coefficient on the order of -0.10 .

Methods Input*Gradient and Integrated Gradients perform very similarly, both capturing the ground truth very closely. Indeed, both methods capture the positive patterns over eastern Pacific and the southeastern Indian Oceans, and the negative patterns over the Atlantic Ocean. The pattern correlation with the ground truth for both methods is on the order of 0.8 , indicating the very high agreement.

Regarding LRP methods, first, our results confirm the arguments in [25],[47], that the Deep Taylor leads to similar results with the $LRP_{\alpha=1, \beta=0}$. Second, both methods return only positive contributions which is consistent with (7). Indeed, since $\alpha = 1, \beta = 0$, and the ratio $\frac{z_{ij}^+}{z_j^+}$ is always positive, the sign of the NN prediction is propagated back to all neurons and to all features of the input. Because the NN prediction is positive in Fig. 3, then it is expected that $LRP_{\alpha=1, \beta=0}$ (and Deep Taylor) returns only positive contributions (see also remarks by [49]). What is not so intuitive is the fact that the $LRP_{\alpha=1, \beta=0}$ seems to highlight all important features, independent of the sign of their contribution (compare with ground truth). Given that, by construction of (7), $LRP_{\alpha=1, \beta=0}$ considers only positive preactivations [24], one might assume that it will only highlight the features that positively contribute to the prediction. However, the results in Fig. 3 show that the method highlights the entire Atlantic Ocean with a positive contribution. This is problematic, since the ground truth heatmap clearly indicates that this region is contributing negatively to the response y_n in this example. The issue of $LRP_{\alpha=1, \beta=0}$ in highlighting all features independent of whether they are contributing positively

or negatively to the prediction has been very recently shown in other applications of XAI as well [49]. Interestingly though, we have established that this issue is not present when one applies the $LRP_{\alpha=1, \beta=0}$ to explain a linear model (not shown). In this case, the $LRP_{\alpha=1, \beta=0}$ returns only the features with positive contribution. This seems to suggest that the issue of mixing positive and negative contributions depends on the complexity of the model that is being explained, and is more likely to occur as the model complexity increases.

Lastly, when using the LRP_z rule, the attribution heatmap very closely captures the ground truth, and it exhibits a very high pattern correlation on the order of 0.82 . The results are very similar to those of the methods Input*Gradient and Integrated Gradients, making these three methods the best performing ones for this example sample. This is consistent with the discussion in [34], which showed the equivalence of the methods Input*Gradient and LRP_z in cases of NNs with ReLU activation functions, as in our study.

Similar remarks with those based on Fig. 3 can be made based on Fig. 4, which presents the ground truth and the estimated attributions for another example, where the response is negative and equal to $y_n = -0.1474$. The prediction of the NN for this example is -0.1416 . First, methods Gradient and Smooth Gradient perform poorly again, with correlations with the ground truth on the order of 0.03 and 0.07 , respectively. Methods Input*Gradient and Integrated Gradients are the best performing ones together with the method LRP_z , all of which strongly correlate with the ground truth (correlation coefficients on the order of $0.8-0.85$). The method Deep Taylor does not return any attributions since is defined for only positive predictions [25], a fact that limits its application to classification problems or regression problems with positive predictand variables only. Lastly, in accordance with the remarks from Fig. 3, the attributions from $LRP_{\alpha=1, \beta=0}$ are all negative, since the NN prediction for this example is negative.

Also, it is again evident that $LRP_{\alpha=1,\beta=0}$ highlights all important features and not only the ones that are positively contributing to the prediction. In general, one should be cautious when using this rule, keeping always in mind that, i) it might propagate the sign of the prediction back to all the relevances of the input layer and ii) it is likely to mix positive and negative contributions.

B. Quantitative Summarizing Statistics

In Fig. 5 we present histograms of the correlation coefficients between different XAI methods and the ground truth for all 100,000 validation samples. In this way one can inspect the performance of each of the XAI methods based on all validation samples and verify the specific remarks that were highlighted above.

First, in panel Fig. 5a, we present results from the same XAI method (i.e., Input*Gradient) but applied to the two different models, the NN and the linear regression model. Thus, any difference in the performance comes solely from how well the corresponding models have captured the true underlying function F . The NN more closely approximates the function F since the pattern correlations are systematically higher than the ones for the linear model, consistent with the much better prediction performance of the NN. The average pattern correlation between the attribution of the NN and the ground truth is on the order of 0.8, whereas for the linear model it is on the order of 0.55.

Second, in panel Fig. 5b, we present results for all gradient-based methods applied to the NN. Methods Gradient and Smooth Gradient perform very poorly (both exhibit almost zero average correlation with the ground truth), while methods Input*Gradient and Integrated Gradients perform equally well, exhibiting an average correlation with the ground truth around 0.8.

Last, in panel Fig. 5c, we present results for LRP. The LRP_z rule is seen to be the best performing with very similar performance to the Input*Gradient and Integrated Gradients methods (as theoretically expected for this model setting; see [34]). The corresponding average correlation coefficient is on the order of 0.8. Regarding the $LRP_{\alpha=1,\beta=0}$ rule, we present two curves. The first curve (black curve in Fig. 5c) corresponds to correlation with the ground truth after we have set all the negative contributions in the ground truth to zero. The second curve (blue curve) corresponds to correlation with the absolute value of the ground truth. For both curves we multiply the correlation value with -1 when the NN prediction was negative, to account for the fact that the prediction's sign is propagated back to the attributions. Our results show that when correlating with the absolute ground truth (blue curve), the correlations are systematically higher than when correlating with then nonnegative ground truth (black curve). This result verifies that the issue of $LRP_{\alpha=1,\beta=0}$ highlighting both positive and negative attributions occurs for all the validation samples, further highlighting the need to be cautious when using this rule.

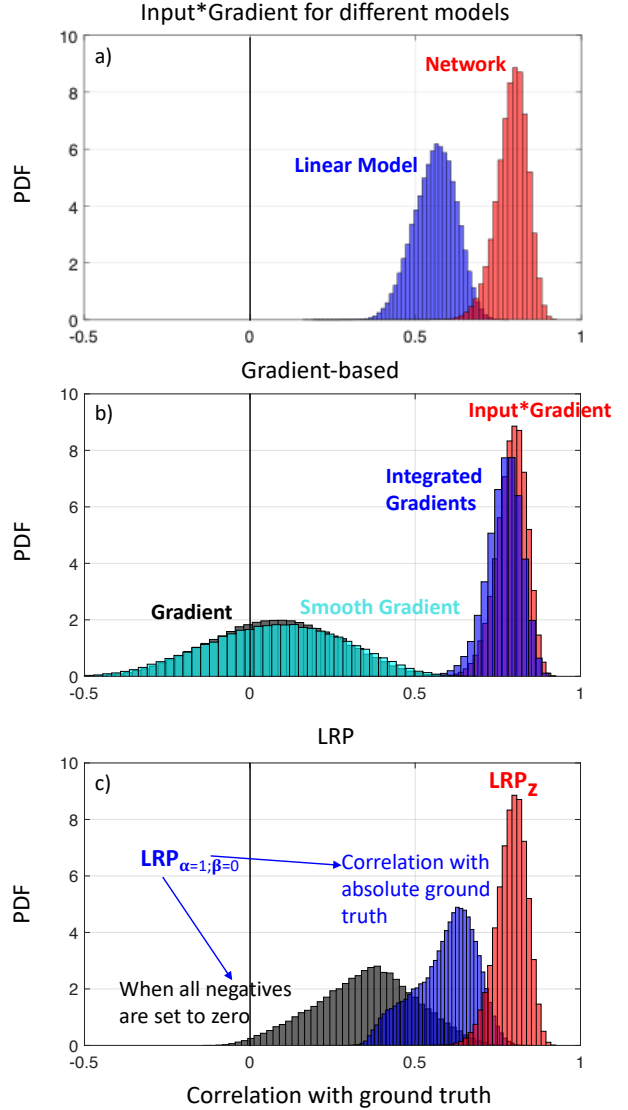


Fig. 5. Summary of the performance of different XAI methods. Histograms of the correlation coefficients between different XAI heatmaps and the ground truth for 100,000 validation samples.

V. CONCLUSIONS AND FUTURE WORK

The potential for NNs to successfully tackle complex problems in geoscience has become quite evident in recent years. An important requirement for further application of NNs in geoscience is their robust explainability, and newly developed XAI methods show very promising results for this task. However, the assessment of XAI methods often requires the scientist to know what the attribution should look like and is often subjective. Also, applicable attribution benchmark datasets are rarely available, especially for regression problems.

Here, we introduce a new framework to generate synthetic attribution benchmarks to test XAI methods. In our proposed framework, the ground truth of the attribution of the output to the input is objectively derivable for any sample. This framework is based on the use of additively separable functions, where the response $Y \in \mathbb{R}$ to the input $\mathbf{X} \in \mathbb{R}^d$ is the sum of local responses. The local responses may have any functional form, while spatial functional dependence can also be enforced.

Independent of how complex the local functions might be, the true attribution is always derivable. As an example, we create 10^6 samples using local piece-wise linear functions and utilize a fully connected NN to learn the underlying function. Based on the true attribution, we then quantitatively assess the performance of various common XAI methods.

In general, our results suggest that methods Gradient and Smooth Gradient may be suitable for estimating the sensitivity of the output to the input, but this is not necessarily equivalent to the attribution. We also reveal some potential issues in deriving the attribution when using the $LRP_{\alpha=1, \beta=0}$ rule. For the specific setup used here, the methods Input*Gradient, Integrated Gradients, and the LRP_z rule all very closely capture the true function F and are the best performing XAI methods considered here.

In summary, in this study we demonstrated the benefits of attribution benchmarks for the identification of possible systematic pitfalls of XAI, and introduced a framework to create such benchmarks with emphasis on geoscience. Clearly, this is only the beginning of a larger research effort. In the future, we plan to extend this work to assess a larger range of XAI methods, using different deep learning models (convolutional NNs, recurrent NNs, etc.) and to derive other forms of nonlinear local functions encountered more frequently in the geosciences (e.g., based on ordinary differential equations). We believe that a common use and engagement of such attribution benchmarks by the geoscientific community can lead to a more cautious and accurate application of XAI methods to physical problems. Such efforts will increase model trust and facilitate scientific discovery.

REFERENCES

- [1] Y. LeCun, Y. Bengio, G. Hinton, "Deep learning," *Nature*, vol. 521, pp. 436-444, 2015.
- [2] M. Reichstein *et al.*, "Deep learning and process understanding for data-driven Earth system science," *Nature*, vol. 566, pp. 195-204, 2019.
- [3] C. Shen, "A transdisciplinary review of deep learning research and its relevance for water resources scientists," *Water Resources Research*, vol. 54, pp. 8558-8593, 2018.
- [4] D. J. Lary *et al.*, "Machine learning in geosciences and remote sensing," *Geoscience Frontiers*, vol. 7, no. 1, pp. 3-10, 2016.
- [5] M. Sit *et al.*, "A comprehensive review of deep learning applications in hydrology and water resources," arXiv preprint, <https://arxiv.org/abs/2007.12269>, 2020.
- [6] K. J. Bergen *et al.*, "Machine learning for data-driven discovery in solid Earth geoscience," *Science*, vol. 363, no. 6433, eaau0323, 2019.
- [7] A. Karpatne *et al.*, "Machine learning for the Geosciences: Challenges and opportunities," *IEEE Trans. Knowledge and Data Engin.*, vol. 31, no. 8, pp. 1544-1554, 2018.
- [8] E. A. Barnes *et al.*, "Viewing forced climate patterns through an AI Lens," *Geophysical Research Letters*, vol. 46, pp. 13389-13398, 2019.
- [9] D. Rolnick *et al.*, "Tackling climate change with machine learning," arXiv preprint, <https://arxiv.org/abs/1906.05433>, 2019.
- [10] Y. G. Ham, J. H. Kim, J. J. Luo, "Deep learning for multi-year ENSO forecasts," *Nature*, vol. 573, pp. 568-572, 2019.
- [11] D. Reinsel, J. Gantz, J. Rydning, "The digitization of the world: from edge to core" IDC, Framingham, MA, USA, White Paper Doc# US44413318, 2018, p. 28. [Online]. Available: <https://www.seagate.com/files/www-content/our-story/trends/files/idc-seagate-dataagewhitepaper.pdf>
- [12] H. Guo, "Big Earth data: A new frontier in Earth and information sciences," *Big Earth Data*, vol. 1, no. 1-2, pp. 4-20, 2017.
- [13] J. T. Overpeck *et al.*, "Climate data challenges in the 21st century," *Science*, vol. 331, no. 6018, pp. 700-702, 2011.
- [14] A. Agapiou, "Remote sensing in a petabyte-scale: satellite data and heritage Earth Engine© applications," *International Journal of Digital Earth*, vol. 10, no. 1, pp. 85-102, 2017.
- [15] S. Lapuschkin *et al.*, "Unmasking clever Hans predictors and assessing what machines really learn," *Nature Communications*, vol. 10, no. 1096, 2019.
- [16] I. Ebert-Uphoff, K. Hilburn, "Evaluation, tuning, and interpretation of neural networks for working with images in meteorological applications," *Bulletin of the American Meteorological Society*, vol. 101, no. 12, pp. E2149-E2170, 2020.
- [17] A. Shrikumar *et al.*, "Not just a black box: Learning important features through propagating activation differences," arXiv preprint, <https://arxiv.org/abs/1605.01713>, 2016.
- [18] A. Shrikumar, P. Greenside, A. Kundaje, "Learning important features through propagating activation differences," arXiv preprint, <https://arxiv.org/abs/1704.02685>, 2017.
- [19] D. Smilkov *et al.*, "SmoothGrad: removing noise by adding noise," arXiv preprint, <https://arxiv.org/abs/1706.03825>, 2017.
- [20] M. D. Zeiler, R. Fergus, "Visualizing and understanding convolutional networks," arXiv preprint, <https://arxiv.org/abs/1311.2901>, 2013.
- [21] J. T. Springenberg *et al.*, "Striving for simplicity: The all convolutional net," arXiv preprint, <https://arxiv.org/abs/1412.6806>, 2015.
- [22] P.-J. Kindermans *et al.*, "Learning how to explain neural networks: PatternNet and PatternAttribution," arXiv preprint, <https://arxiv.org/abs/1705.05598>, 2017.
- [23] M. Sundararajan, A. Taly, Q. Yan, "Axiomatic attribution for deep networks," arXiv preprint, <https://arxiv.org/abs/1703.01365>, 2017.
- [24] S. Bach *et al.*, "On pixel-wise explanations for non-linear classifier decisions by layer-wise relevance propagation," *PLoS One*, vol. 10, no. 7, e0130140, 2015.
- [25] G. Montavon *et al.*, "Explaining nonlinear classification decisions with deep Taylor decomposition," *Pattern Recognition*, vol. 65, pp. 211-222, 2017.
- [26] M. Ancona *et al.*, "Gradient-based attribution methods," in *Explainable AI: Interpreting, Explaining and Visualizing Deep Learning*, pp. 169-191, Springer, 2019.

- [27] A. Das, P. Rad, “Opportunities and challenges in explainable artificial intelligence (XAI): A survey,” arXiv preprint, <https://arxiv.org/abs/2006.11371>, 2020.
- [28] V. Buhmester, D. Münch, M. Arens, “Analysis of explainers of black box deep neural networks for computer vision: A survey,” arXiv preprint, <https://arxiv.org/abs/1911.12116>, 2019.
- [29] E. Tjoa, C. Guan, “A survey on explainable artificial intelligence (XAI): Towards medical XAI,” arXiv preprint, arXiv:1907.07374, 2019.
- [30] A. McGovern *et al.*, “Making the black box more transparent: Understanding the physical implications of machine learning,” *Bulletin of the American Meteorological Society*, vol. 100, no. 11, pp. 2175-2199, 2019.
- [31] B. A. Toms, E. A. Barnes, I. Ebert-Uphoff, “Physically interpretable neural networks for the geosciences: Applications to Earth system variability,” *Journal of Advances in Modeling Earth Systems*, vol. 12, e2019MS002002, 2020.
- [32] E. A. Barnes *et al.*, “Indicator patterns of forced changed learned by an artificial neural network,” *Journal of Advances in Modeling Earth Systems*, vol. 12, e2020MS002195, 2020.
- [33] A.-K. Dombrowski *et al.*, “Towards robust explanations for deep neural networks,” arXiv preprint, <https://arxiv.org/abs/2012.10425>, 2020.
- [34] M. Ancona *et al.*, “Towards better understanding of gradient-based attribution methods for deep neural networks,” arXiv preprint, <https://arxiv.org/abs/1711.06104>, 2018.
- [35] P.-J. Kindermans *et al.*, “The (un)reliability of saliency methods,” arXiv preprint, <https://arxiv.org/abs/1711.00867>, 2017.
- [36] C. Rudin “Stop explaining black box machine learning models for high stakes decisions and use interpretable models instead,” *Nature Machine Learning*, vol 1, pp. 206-215, 2019.
- [37] Y. Lecun *et al.*, “Gradient-based learning applied to document recognition,” *Proceedings of the IEEE*, vol. 86, no. 11, pp. 2278-2324, 1998.
- [38] O. Russakovsky *et al.*, “ImageNet large scale visual recognition challenge,” arXiv preprint, <https://arxiv.org/abs/1409.0575>, 2015.
- [39] V. Petsiuk, A. Das, K. Saenko, “RISE: Randomized input sampling for explanation of black-box models,” arXiv preprint, <https://arxiv.org/abs/1806.07421>, 2018.
- [40] W. Samek *et al.*, “Evaluating the visualization of what a deep neural network has learned,” *IEEE Transactions on Neural Networks and Learning Systems*, vol. 28, no. 11, 2017.
- [41] Z. Qi, S. Khorram, L. Fuxin, “Visualizing deep networks by optimizing with integrated gradients,” arXiv preprint, <https://arxiv.org/abs/1905.00954>, 2020.
- [42] M. L. Leavitt, A.S. Morcos, “Towards falsifiable interpretability research,” arXiv preprint, <https://arxiv.org/abs/2010.12016>, 2020.
- [43] T. DelSole, A. Banerjee, “Statistical seasonal prediction based on regularized regression,” *Journal of Climate*, vol. 30, no. 4, pp. 1345-1361, 2017.
- [44] A. Stevens *et al.*, “Graph-guided regularized regression of Pacific Ocean climate variables to increase predictive skill of southwestern US winter precipitation,” *Journal of Climate*, vol. 34, no. 2, pp. 737-754, 2021.
- [45] J. Feng, W. Chen, Y. Li, “Asymmetry of the winter extratropical teleconnections in the Northern Hemisphere associated with two types of ENSO,” *Clim. Dyn.*, vol. 48, pp. 2135-2151, 2017.
- [46] T. Zhang, J. Perlwitz, M. P. Hoerling, “What is responsible for the strong observed asymmetry in teleconnections between El Niño and La Niña?,” *Geophysical Research Letters*, vol. 41, pp. 1019-1025, 2014.
- [47] W. Samek *et al.*, “Interpreting the predictions of complex ML models by layer-wise relevance propagation,” arXiv preprint, <https://arxiv.org/abs/1611.08191>, 2016.
- [48] J. Adebayo *et al.*, “Sanity checks for saliency maps,” arXiv preprint, <https://arxiv.org/abs/1810.03292>, 2020.
- [49] M. Kohlbrenner *et al.*, “Towards best practice in explaining neural network decisions with LRP,” 2020 International Joint Conference on Neural Networks (IJCNN), Glasgow, UK, pp. 1-7, 2020.